Earth and Planetary Science Letters 544 (2020) 116389

Contents lists available at ScienceDirect

Earth and Planetary Science Letters

www.elsevier.com/locate/epsl

The formation of Enceladus' Tiger Stripe Fractures from eccentricity tides

Alyssa Rose Rhoden [a,*,1], Terry A. Hurford [b], Joseph Spitale [c], Wade Henning [d], Eric M. Huff [e], Michael T. Bland [f], Stan Sajous [g]

[a] Southwest Research Institute, Boulder, CO, United States of America
[b] NASA Goddard Space Flight Center, Code 698, Greenbelt, MD, United States of America
[c] Planetary Science Institute, Tucson, AZ, United States of America
[d] Department of Astronomy, University of Maryland – College Park, College Park, MD, United States of America
[e] NASA Jet Propulsion Laboratory, Pasadena, CA, United States of America
[f] Astrogeology Science Center, U. S. Geological Survey, Flagstaff, AZ, United States of America
[g] Sajous Consulting, LLC, Denver, CO, United States of America

ARTICLE INFO

Article history:
Accepted 2 June 2020
Available online 12 June 2020
Editor: W.B. McKinnon

Keywords:
Enceladus
satellite tides
ocean worlds
tectonics

ABSTRACT

Enceladus has a young, tectonically active south polar region, which is erupting material from a prominent set of fractures called Tiger Stripes. No comparable activity is observed at the north pole, which is heavily cratered with limited tectonism. Given the many lines of evidence supporting a global ocean under Enceladus' icy shell, the reason for the dichotomy in geologic activity is unclear. We model the formation of the Tiger Stripes as tidally-driven fractures and examine the magnitudes of tidal stresses with different ice shell structures in order to explore whether and how tidal stress might explain Enceladus' distribution of tectonic activity. We find that eccentricity-driven tidal stresses would produce fractures of nearly identical orientations to the observed Tiger Stripe Fractures and that a 10-km difference in ice shell thickness between the north and south poles can result in substantially different tidal stress magnitudes, providing a natural explanation for the hemispheric dichotomy in tectonic activity on Enceladus. Finally, we synthesize these results with Enceladus' global geologic record to offer insight into the evolution of this enigmatic moon.

1. Introduction

Enceladus, one of Saturn's smallest and closest moons, has a pervasively fractured south pole that is actively jetting material into space (Porco et al., 2006; Spencer et al., 2006; Patthoff and Kattenhorn, 2011; Crow-Willard and Pappalardo, 2015) and a heavily cratered north pole with comparatively little tectonism (Martin, 2016). The most prominent features in the south polar terrain (SPT) are the four, roughly parallel, Tiger Stripe Fractures (TSFs). Tidal stresses caused by Enceladus' forced orbital eccentricity may have been involved in the formation of the TSFs (e.g., Nimmo et al., 2007), although a non-tidal origin has also been proposed (e.g., Yin and Pappalardo, 2015). Plumes emanate from the TSFs (Spitale and Porco, 2007; Porco et al., 2014; Spitale et al., 2015; Helfenstein and Porco, 2015), and their eruptive output varies with Enceladus' tidal cycle (Hedman et al., 2013), implying that tides control the eruptions. However, explaining the timing has proved difficult (Nimmo et al., 2007, 2014; Hurford et al., 2007; Behounkova et al., 2015; Kite and Rubin, 2016; Behounkova et al., 2017). Identifying a mechanism for generating Enceladus' active SPT, while leaving an ancient surface at its north pole, is one of the most intriguing challenges left in the wake of the *Cassini* mission.

Assessing the magnitude of tidal stress depends on the responsiveness and structure and of Enceladus' interior, which is still uncertain. Model fits to observed librations support a global ocean and average ice shell thickness of 21 to 26 km, assuming an elastic shell; accounting for viscosity, the ice shell could be up to 7 km thinner (Thomas et al., 2016). Isostacy arguments imply that the ice shell is thinner than the global average at the south pole, with an estimate of ~13 km (Thomas et al., 2016). Fits to *Cassini* gravity measurements provide a range of values, depending on model as-

* Corresponding author at: Southwest Research Institute, 1050 Walnut St. #300, Boulder, CO 80302, United States of America.
E-mail address: Alyssa@boulder.swri.edu (A.R. Rhoden).
[1] Previously published under the surname Sarid.

https://doi.org/10.1016/j.epsl.2020.116389
0012-821X/

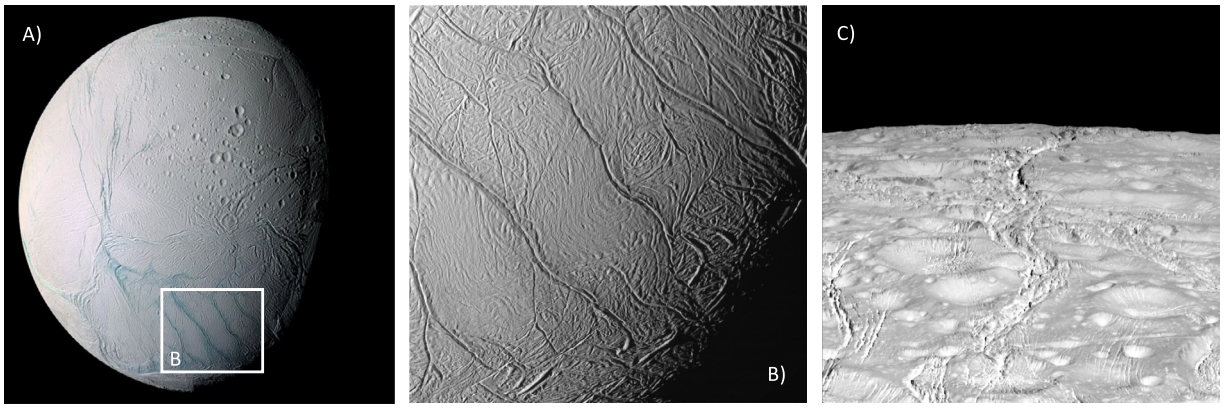

Fig. 1. Enceladus' diverse geology is apparent even from the (A) global view, in which the Tiger Stripe Fractures (shown up close in B) and their surrounding fractures can be seen toward the bottom of the image. (C) The north pole, which falls in the center of this image, is heavily cratered with fractures that display very different morphology than those in the south. Some fractures appear to have propagated around preexisting craters, while others are focused by craters. (A) PIA06249, false color composite, ~670 m/pix; (B) PIA06247, 122 m/pix; (C) PIA19660, 35 m/pix.

sumptions, from roughly 10 km or thicker at the south pole (Iess et al., 2014; McKinnon, 2015; Beuthe et al., 2016) to less than 5 km (Beuthe et al., 2016; Cadek et al., 2016, 2019); the ice shell at the north pole is always thicker than at the south pole in these models. It is also possible that Enceladus' ice shell was thinner in the past, either globally or locally, which is supported by the pattern of ice shell thickness derived from gravity data (Cadek et al., 2019).

Here, we take a detailed look at the role of eccentricity-driven (i.e., diurnal) tides in the formation of the Tiger Stripe Fractures and how Enceladus' interior structure and shell thickness variations might have shaped the tectonics of the south and north polar regions. We explore failure assumptions that were not considered in previous work. Specifically, we test the assumption that Enceladus' ice shell fails at a consistent threshold throughout the SPT, which can be lower than the maximum stress achieved in any one location. We restrict our study to the present-day eccentricity of 0.0047 and do not include stress from non-synchronous rotation as it has already been examined by Patthoff et al. (2019).

2. Interpretations of Enceladus' geologic record

A striking feature of Enceladus' global geologic record (Fig. 1A) is its regionally and temporally heterogeneous tectonic activity (e.g. Crow-Willard and Pappalardo, 2015). The most extensive and youngest region of tectonic activity is seen near the south pole (Fig. 1B, Fig. 2A). This region has been extensively mapped (Crow-Willard and Pappalardo, 2015; Patthoff and Kattenhorn, 2011; Yin and Pappalardo, 2015; Helfenstein and Porco, 2015) and is made up of a background of densely-packed fractures, overlain by four prominent fractures: Alexandria, Baghdad, Cairo, and Damascus Sulcus (i.e. the Tiger Stripes), which are also the sources of the plumes (Spitale and Porco, 2007; Porco et al., 2014; Spitale et al., 2015; Helfenstein and Porco, 2015). The region displays various textures, perhaps affected by the addition of plume material over time, including raised ridges along the fractures and topographic features such as "shark fins" that appear alongside or between some ridges but not others (Helfenstein and Porco, 2015). Folds, normal faults, and strike-slip faults have also been identified (Crow-Willard and Pappalardo, 2015; Yin and Pappalardo, 2015; Helfenstein and Porco, 2015; Martin, 2016). The whole south polar terrain appears to be depressed relative to its surroundings; a system of bounding troughs, concentric to the south pole, delineates the depressed terrain. In some places, these troughs develop into northward-trending systems of fractures. No craters have been identified within the SPT.

Some older areas of tectonism are found in equatorial regions of the leading and trailing hemispheres, which bear some similarities to the fracture systems within the SPT, including sets of bounding fractures (Crow-Willard and Pappalardo, 2015). However, the regions are more heavily cratered, display less dense networks of fractures, and are not associated with any observed plumes. Currently unknown is whether differences between the leading/trailing tectonized terrains and the SPT are due to their formation mechanism, their physical/thermal characteristics, their ages, or some combination of these. In addition to the tectonized terrains, some strike-slip faults and pit chains are distributed across Enceladus (Martin, 2016). The presence of tectonized terrains along the equator and other spatially distributed tectonic activity implies that the material strength of Enceladus' ice does not vary enough to inhibit fracture formation outside of the SPT.

The northern polar region displays much less tectonic activity than any other area (Crow-Willard and Pappalardo, 2015). Fractures at the north pole tend to be troughs or scarps without raised flanking ridges (Fig. 1C). They often interact with preexisting terrain such as craters, which may even focus some fractures (e.g., Kinczyk et al., 2017). The north pole is the most heavily cratered, and thus inferred to be the oldest, of Enceladus' terrains. However, the appearance of pit chains and fractures that intersect craters both suggest that even Enceladus' ancient terrains are still geologic active to some extent (Kinczyk et al., 2017; Martin, 2016).

TSF formation has not been studied as extensively as their associated plumes, though tidal stresses are often invoked as the most likely mechanism (e.g., Hurford et al., 2007; Nimmo et al., 2007, 2014; Patthoff and Kattenhorn, 2011; Porco et al., 2014; Behounkova et al., 2015; Patthoff et al., 2019). Patthoff et al. (2019) explored the formation of the TSFs in response to tidal stresses from non-synchronous rotation (NSR) of Enceladus' ice shell relative to its silicate interior. The TSF orientations are not consistent with the present day NSR stress field, implying that the ice shell has rotated by ~45° since they formed. The decrease in magnitude of NSR-related tidal stress with increasing shell thickness could also explain the lack of fracturing elsewhere on Enceladus. This result builds upon the previous estimate of NSR from analysis of the older fracture sets in the SPT (Patthoff and Kattenhorn, 2011), although that interpretation is based on the assumption that all cracks of similar orientation are the same age. More analysis is required to determine whether diurnal stresses are sufficient to explain the observed orientations of the TSFs, thereby alleviating the need to invoke rotation and stresses from NSR.

Hemingway et al. (2020) proposed that a combination of ice shell cooling, ocean pressurization, and diurnal tidal stress led to

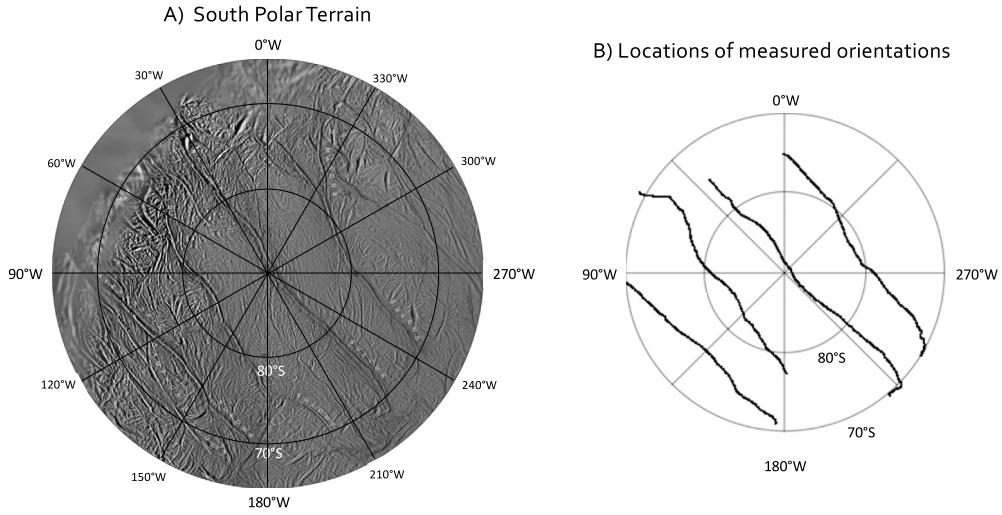

Fig. 2. A) The south polar terrain of Enceladus is heavily tectonized and free of craters. The most distinctive, and likely youngest, features are four, roughly parallel fractures, dubbed Tiger Stripes, from which Enceladus' plumes emanate. B) We used the fracture orientations at each of the 2395 points shown here to assess models of fracture formation due to diurnal tidal stress.

the formation of Baghdad Sulcus, which relieved stress and prevented fractures from forming elsewhere, particularly at the north pole. Plume material then erupted from the fracture, loaded the flanking region, imposed bending stresses on the SPT, and eventually led to failure and the creation of parallel fractures that we observe as the Tiger Stripes. One drawback to this model is that it produces only one fracture, which leaves no mechanism to explain the tectonized terrains in the leading and trailing hemispheres or the numerous fractures underlying the TSFs. In addition, the tidal stresses that control the orientation of Baghdad were not explicitly modeled.

An alternative model (Yin and Pappalardo, 2015; Yin et al., 2016) suggests that the TSFs formed as strike-slip faults in response to large-scale motion and deformation of the south polar region. This result was based on detailed structural mapping using high-resolution imagery and may explain several characteristics of the SPT that other models do not, such as the bounding troughs, attendant fracture systems, and strike-slip faults. However, as pointed out by Hemingway et al. (2020), forming the TSFs as shear fractures rather than tensile ones makes it difficult to explain the ongoing eruptions of plume material that suggest these fractures are open conduits over much of their lengths.

Determining whether a tidal stress model can explain the orientations of the TSFs at least as well as Yin and Pappalardo (2015) is a key driver of this work. In particular, we assess whether eccentricity-driven tidal stress can match the orientations of the TSFs, without invoking stress or rotation from NSR or requiring stress relief to inhibit other fracturing, which is difficult to reconcile with the tectonism observed in the leading and trailing hemispheres and the older tectonic features within the SPT. An additional goal of this work is to test whether a drop in tidal stress magnitudes due to the inferred difference in shell thickness between the south and north poles could explain the dichotomy in tectonic activity, similar to the analysis of Patthoff et al. (2019) using NSR stresses.

3. Methods

We use *Cassini* images to collect latitude and longitude information at 2395 points along the most prominent branches of the TSFs (Fig. 2A, B; SOM). Analysis of cross-cutting relationships within the SPT suggests that the more prominent TSFs are younger than the other fracture segments (Patthoff and Kattenhorn, 2011), so they may have formed under different stress conditions than the less prominent features. We compute stress at the midpoint between neighboring mapped points. The fracture orientation is taken to be the vector connecting the two adjacent mapped points, where orientation increases clockwise from north at 0°W longitude. These orientations are compared to the predicted orientations from the tidal models, which depend on the interior structure and assumed failure criterion.

We compute diurnal tidal stresses in a rheologically-layered body, following the formulation of Jara-Orué and Vermeersen (2011), which utilizes the propagator matrix method to determine the responses of internal layers to tidal forcing. The first step in the calculations is to determine the tidal response of a satellite by calculating the Love numbers and the strengths of normal modes that correspond to internal layer interfaces. The tidal response depends mainly on the thickness and viscosity that we assume for each layer. In the second step, we use the tidal response parameters as inputs into the tidal stress calculations, which depend mainly on the forcing frequency (mean motion in this case), eccentricity, and other orbital parameters. The output of these calculations is the tidal stress tensor, at a given location through time, which can be decomposed into principal stress components. Our methodology is described in detail in Rhoden et al. (2015) and Rhoden et al. (2017), in which all of the equations are shown in Appendix A. All parameter values necessary to reproduce our results are given in Tables 1, 2, and in the SOM.

The equations we employ were derived for a five-layer body in which two layers are assumed to be fluid: a core and a subsurface ocean. To eliminate the innermost fluid layer would require that an entirely new system of equations be derived and solved. However, as in our previous work (Rhoden et al., 2015, 2017), we find that reducing the thickness of the innermost layer (i.e., the liquid core) to a radius of 10 km, and assigning it a density similar to that of the overlying silicate layer, is equivalent to using a four-layer model with a solid silicate innermost layer. We have validated our numerical tools against published results for Europa (Jara-Orué and Vermeersen, 2011) and against output from the publicly-available tidal stress software, SatStress, which is based on the equations of Wahr et al. (2009). Due to differences in the mathematical approach of these two methods and different model assumptions (e.g., compressibility), SatStress and our code, SIMON, produce slightly different stress values, but the differences are small enough that either code should produce the

Table 1
Parameters held constant across all models.

Orbital period		1.37 d
Surface gravity		0.113 m/s^2
Radius		252.1 km
Mass		1.08022 $\times$ 10^{20} kg
Eccentricity		0.0047
Pseudo-core	Thickness	10 km
	Rigidity	0 Pa (liquid)
	Density	2510 kg/m^3
	Viscosity	0 Pa·s (liquid)
Mantle	Thickness	177 km
	Rigidity	6.5 $\times$ 10^{10} Pa
	Density	2490 kg/m^3
	Viscosity	10^{19} Pa·s
Ocean density		1000 kg/m^3
Ice	Rigidity	3.487 $\times$ 10^9 Pa
	Ductile density	999 kg/m^3
	Brittle density	998 kg/m^3
	Brittle layer viscosity	10^{21} Pa·s

same overall results. For a more detailed discussion of the different model assumptions made in tidal stress modeling codes, see Beuthe (2018). While SatStress does provide a framework for computing stresses in four layer models, we prefer to use SIMON, so that we can consistently compare stresses across bodies we have previously evaluated.

The formulation we employ also requires that each of the five layers has uniform thickness, but Enceladus' ice shell is thought to be thicker in the north than in the south and thickest at the equator. Therefore, we make the assumption that stresses calculated for a uniform thickness shell are a good approximation to a local region with that thickness, which is supported by the analysis of Kalousova et al. (2012). For example, we assume that a model with a globally thin shell would produce stresses that are applicable near the south pole, where the shell is likely thin. Whereas, a globally thick shell would be appropriate for stresses at the north pole. Many studies of Enceladus' south pole have used uniform thickness ice shells (e.g., Hurford et al., 2007; Nimmo et al., 2007, 2014; Patthoff and Kattenhorn, 2011; Kalousova et al., 2012; Porco et al., 2014; Behounkova et al., 2015, and Patthoff et al., 2019) when calculating stress at the south pole. Beuthe (2018) and Behounkova et al. (2017) have examined the effects of a variable ice shell on tidal stresses, which we discuss in Section 5.

We compute tidal stresses for a broad range of interior structures that are consistent with estimates in the literature, and models with thinner shells that may be representative of past conditions, particularly at the south pole. All of the interior structures we test include the 10 km liquid silicate "pseudo-core" described above, overlain by a 177 km solid silicate mantle, overlain by a 65 km thick hydrosphere (see Table 1). The hydrosphere is further separated into a global liquid water ocean at the base, a "ductile" lower ice shell, and a "brittle" upper ice shell. We test total ice shell thicknesses of 22 km, 12 km, 1 km, and 500 m (see Table 2), and we compute stresses for a few intermediate cases to better document trends. We presume that the thinner shells ($\leq$5 km) are only relevant for the south polar region.

For the thickest shells, we test models in which the brittle layer thickness is ~10%, 20%, or 30% of the total shell thickness (rounded to the nearest km) and a viscosity for the lower part of the ice shell that is 10^{13}, 10^{14}, or 10^{15} Pa·s. In thinner shells, we always assume the brittle layer is ~10% of the total shell thickness but explore a wider range of lower ductile shell viscosities: 10^{13}, 10^{15}, or 10^{19} Pa·s. Given the limited constraints, we focus on combinations of brittle layer thickness and ductile shell viscosity that are most likely to produce variations in tidal stress. The brittle layer thickness could certainly be larger than the values we test. Increasing it reduces the responsiveness of the ice shell to tidal deformation, and the stress magnitudes converge to high viscosity ductile layer values.

Parameters that are held constant across all models are shown in the SOM. We do not vary any properties of the layers below the ocean. The density of Enceladus' silicate interior, liquid ocean, and ice shell are not well-known. We adopt plausible values that, for a given set of layer thicknesses, match Enceladus' mass. Our past work has shown that tidal stresses are not very sensitive to these values (e.g., Rhoden et al., 2015). In addition, Beuthe (2018) reports minimal deviations in tidal stresses due to differences in the assumed density contrast of the ice shell and ocean.

We note that, if the ice shell is not convecting, our two-layer ice shell model is not a good approximation for the viscosity profile of the shell, a limitation of many established tidal stress models (e.g., SatStress). The low viscosity cases (10^{13} Pa·s) are the least applicable to a conducting shell because we treat the entire thickness of the layer as low viscosity whereas, in reality, the ice would only be at/near the melting-point viscosity near the base of the shell. Hence, if Enceladus' ice is thick, but not convecting, the tidal stresses would likely be closer to the magnitudes we find using higher viscosities because they are closer to the average viscosity of the lower shell.

For now, we have chosen not to incorporate any constraints on Enceladus' interior structure from attempts to match the eruptive output of the plumes from the TSFs (Nimmo et al., 2007, 2014; Hurford et al., 2007; Behounkova et al., 2015, 2017). Those models depend on the largely uncertain mechanical process that links tides with eruptions, and the "best fits" to the temporal variations imply interior structures that are inconsistent with the other *Cassini* observations. It is also possible that the system has evolved in ways that decouple the stress state that created the TSFs from that which governs their current behavior. For example, Behounkova et al. (2017) suggest that the presence of the fault planes formed by the TSFs alter the stress field governing plume eruptions. Similarly, Helfenstein and Porco (2015) considered how fractures that cross-cut the TSFs influence the locations, orientations, and possible timing of erupting jets. Since we are concerned with the formation of the TSFs, the altered stress field and post-failure behavior are not relevant to our analysis.

For each interior structure model, we calculate the principal tidal stresses at every 1° in Enceladus' orbit at each of the 2395 locations at which we measured local fracture orientations. We then identify the most tensile principal stress at each time, and its corresponding orientation, to construct curves of tensile stress magnitude versus orientation throughout an orbit. We also identify the largest tensile stress achieved at any location along the TSFs, and at any time in the orbit, for each interior structure model. We refer to this value as the regional peak stress (RPS) and use it to compare the overall potential for failure across different models. To be clear, this value is merely the peak stress achieved at the points along the TSFs at which we evaluated stress; it may not be the largest tidal stress generated on Enceladus.

We test two different failure conditions with which to determine the predicted orientation of a tidally-driven fracture. First, we assume that failure is most likely to occur at a particular location when the tensile stress there reaches its daily maximum. Patthoff et al. (2019) showed that the orientations associated with the max stress were not consistent with the observed TSF orientations at a few select locations they evaluated. We have chosen to test the max stress criterion against our larger data set to ensure that we are getting similar results and for comparison with the predictions of the other failure criterion we test.

The second criterion we test is that failure is most likely to occur at a consistent stress magnitude at all locations, which can be

Table 2
Parameters, tidal stresses, and predicted orientations for each interior structure.

	Total shell thickness (km)	Ductile layer viscosity (Pa·s)	Brittle layer thickness (km)	Peak stress range at TSFs (rounded to nearest kPa)	Assumed failure threshold (rounded to nearest kPa)		Prevailing orientations, predicted (CW off N at 0°W)	
					2/3 RPS	3/4 RPS	2/3 RPS	3/4 RPS
	22	1.00E+15	6	13 - 16	11	12	136.7 +/- 2.9°	141.2 +/- 4.0°
	22	1.00E+15	4	13 - 16	11	12	136.7 +/- 2.9°	141.2 +/- 4.0°
	22	1.00E+15	2	13 - 16	11	12	136.7 +/- 2.9°	141.1 +/- 5.6°
	22	1.00E+14	6	15 - 19	13	14	135.7 +/- 2.8°	140.1 +/- 5.2°
	22	1.00E+14	4	15 - 19	13	14	136.0 +/- 2.8°	140.4 +/- 3.9°
	22	1.00E+14	2	15 - 19	13	14	136.4 +/- 2.8°	140.8 +/- 4.7°
F	22	1.00E+13	6	41 - 49	33	37	131.2 +/- 2.9°	135.6 +/- 3.0°
	22	1.00E+13	4	53 - 64	42	48	131.2 +/- 2.3°	135.4 +/- 2.9°
	22	1.00E+13	2	70 - 85	57	64	132.6 +/- 2.4°	136.8 +/- 3.1°
	12	1.00E+15	3	22 - 27	18	20	133.8 +/- 2.6°	138.2 +/- 5.4°
	12	1.00E+15	2	22 - 27	18	20	133.8 +/- 2.6°	138.2 +/- 5.6°
A	**12**	**1.00E+15**	**1**	**22 - 27**	**18**	**20**	**134.3 +/- 2.6°**	**138.8 +/- 5.7°**
	12	1.00E+14	3	26 - 31	21	24	133.4 +/- 2.5°	137.8 +/- 3.4°
	12	1.00E+14	2	26 - 32	21	24	133.6 +/- 2.5°	138.0 +/- 3.7°
	12	1.00E+14	1	26 - 32	21	24	133.7 +/- 2.6°	138.2 +/- 3.5°
	12	1.00E+13	3	70 - 83	55	62	130.7 +/- 2.4°	135.1 +/- 3.0°
	12	1.00E+13	2	88 - 105	70	78	130.5 +/- 6.5°	135.1 +/- 3.0°
B	**12**	**1.00E+13**	**1**	**113 - 135**	**90**	**102**	**131.6 +/- 3.7°**	**136.1 +/- 3.1°**
C	**5**	**1.00E+13**	**0.5**	**187 - 221**	**147**	**165**	**130.3 +/- 4.8°**	**135.0 +/- 3.0°**
	3	1.00E+13	0.3	237 - 279	186	209	129.7 +/- 8.5°	134.8 +/- 3.0°
	1	1.00E+19	0.1	170 - 200	133	150	130.1 +/- 6.6°	134.8 +/- 3.0°
	1	1.00E+15	0.1	329 - 386	257	290	129.3 +/- 7.7°	134.5 +/- 2.9°
	1	1.00E+13	0.1	329 - 386	258	290	129.3 +/- 7.6°	134.5 +/- 2.9°
D	**0.5**	**1.00E+19**	**0.05**	**234 - 275**	**184**	**207**	**129.7 +/- 8.1°**	**134.6 +/- 3.0°**
	0.5	1.00E+15	0.05	349 - 409	273	307	129.3 +/- 7.5°	134.5 +/- 2.9°
E	**0.5**	**1.00E+13**	**0.05**	**349 - 410**	**273**	**307**	**129.3 +/- 7.4°**	**134.5 +/- 2.9°**

RPS: Regional peak stress; CW: Clockwise; TSFs: Tiger Stripe Fractures.

a value less than the daily maximum stress achieved at any one location. This assumption better reproduces the orientations of lineaments on Europa than a max stress model (Rhoden and Hurford, 2013). However, it poses some challenges when comparing interior models because the tidal stresses vary by more than an order of magnitude across different models. We expect that the failure threshold of Enceladus' ice has a specific value (e.g., 100 kPa), but for the purposes of testing our whole suite of models, we select a threshold relative to the RPS. In our initial tests, we generated predictions at 1/2, 2/3, 3/4, and 9/10 of the RPS. These tests revealed that thresholds of 2/3 and 3/4 of the RPS produced the best results and that using a threshold of 1/2 produced far worse results than other thresholds.

For each TSF point, we identify the predicted fracture orientation corresponding to the maximum daily stress at that location as well as the orientations where the stress increases past the threshold (either 2/3 or 3/4 of the RPS). These values are used to create histograms for each interior structure and failure criterion. We also create a histogram of the observed orientations. We then apply a Gaussian fit to each histogram, using the standard python "norm.fit" function, and compare the peak values from the fits, which we refer to as the prevailing orientations.

To determine whether differences in the ice shell thickness and rheology can explain the increased activity near the south pole relative to the north pole, we compare the RPS's for different interior structures. We first make the simple assumption that failure will occur in any model with an RPS comparable to tidal stresses on Europa, ~100 kPa, and that failure is plausible for an RPS of ≥50 kPa. We discuss how a stronger ice shell would affect our conclusions in subsequent sections.

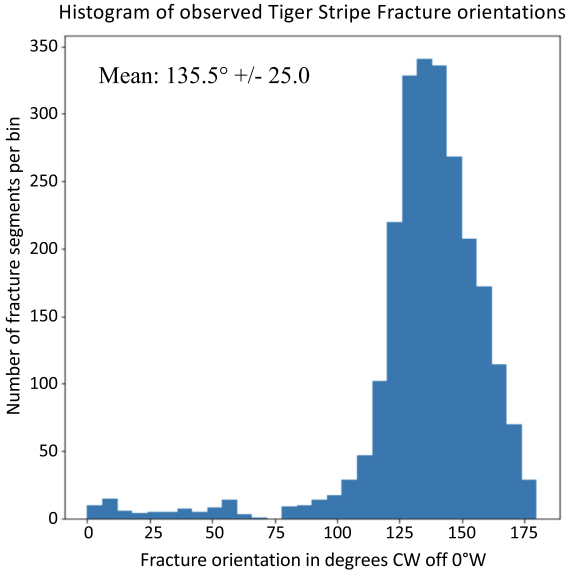

Fig. 3. A histogram of the orientations we measured at 2395 points along the main branches of the TSFs reveals a peak of 135.5° when fit to a Gaussian curve. For the purposes of comparing orientations at different longitudes (in particular, where the TSFs cross the pole), we transformed the measured orientations to be increasing clockwise from the 0°W longitude line rather than the local direction of north.

4. Results

The TSF orientations are strongly clustered (Fig. 3), peaking at 135.5°. Fig. 4 shows the predicted orientations for five interior models (A-E; bold in Table 1), where different colors represent the failure criterion applied (orange: max stress; green: 2/3 RPS; pur-

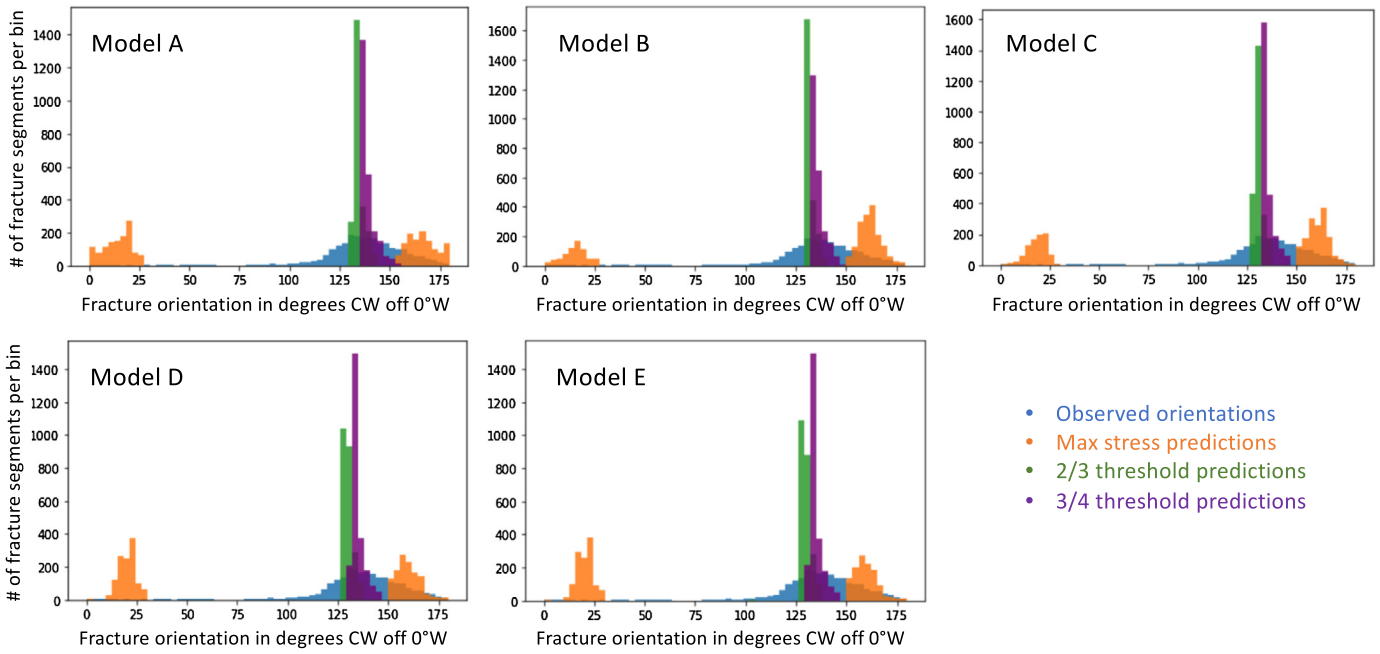

Fig. 4. Histograms of the predicted orientations (i.e. perpendicular to the most tensile principal stress) with each failure criterion (see legend) for the five interior structure models described in Table 2, along with a histogram of the observed orientations. Consistent with previous analyses, we find that the max stress model does a poor job of reproducing the observations. However, adopting a consistent failure threshold matches the peak in the observed histogram almost exactly. (For interpretation of the colors in the figure(s), the reader is referred to the web version of this article.)

ple: 3/4 RPS), along with the observed histogram (blue). Table 2 lists the prevailing orientation value for each model, with each of the threshold criteria.

The max stress model – in which we assume failure occurs at the whatever the daily maximum tensile stress is at each location – does a poor job of matching the observed population. The orientations tend to be roughly north-south, and they come in two clusters, one a bit east of north, and the other west, which each span ∼30° of orientation. Due to the split distribution, we could not determine a meaningful prevailing orientation. These results agree with the findings of Patthoff et al. (2019), that the orientations of the TSFs do not match the orientations produced when tidal stresses reach their daily maximum value.

The threshold failure criterion provides a much better fit to the observations. The 3/4 RPS threshold produces prevailing orientations that are nearly identical to the observations for most interior structures. As demonstrated in Table 2, changing the value we adopt for the failure threshold has a larger effect on the predicted prevailing orientation than the interior structure. For example, the thickest, coolest shell (A) provides the worst fit to the data at 3/4 the RPS at 138.8 ± 5.7°, but it still closely matches with a threshold closer to 2/3 the RPS at 134.3 ± 2.6°. To further illustrate the dependence of the fit on the failure threshold, we also computed prevailing orientations for interior model A at 50% and 90% of the RPS, which resulted in prevailing orientations of 126.23° and 141.8°, respectively.

One major difference between the interior structures is the magnitude of the tidal stresses they generate and the thresholds they imply. Looking across all 27 interior models (Table 2), the RPS ranges from 16 kPa to 410 kPa. Results for a subset of cases are shown graphically in Fig. 5. The lowest stresses are produced in ice shells that are 12 or 22 km thick, with ductile shell viscosities of 10^{14} or 10^{15} Pa·s (green triangles and gray circles in Fig. 5, respectively). These cases have RPS values of 16 to 32 kPa, which is below the minimum value to initiate failure inferred from Europa's tidally-driven fractures. With a viscosity of 10^{13} Pa·s (blue squares in Fig. 5), these thick shells generate stresses from 49 to 135 kPa, depending on the brittle layer thickness, which are comparable to stresses on Europa. For thin shells, 500 m to 5 km total thickness, RPS's are 171 to 410 kPa, larger than those achieved on Europa for all of the ductile shell viscosity values we tested. If we assume that Enceladus' ice has a similar strength to that inferred for Europa, then we would predict failure in all but the coldest, thickest ice shells.

5. Discussion

5.1. Fracture orientations

The close match between the prevailing orientations of the TSFs and those produced with the tidal models strongly supports TSF formation in response to eccentricity-driven tidal stress. We find this good match across all interior structures we tested. The key to matching the orientations was our assumption that the fractures all formed at the same failure threshold. This assumption seems more physically justifiable than assuming fractures form at the local maximum daily stress magnitude, which varies by a few to 10 s of kPa across the TSF locations (Table 2). These results suggest that either tidal stresses of order 100 kPa are sufficient to fracture Enceladus' ice shell or that additional stresses and/or processes contribute to failure (see below).

The range of orientations we predict depends on the variation in tidal stress across the south polar region, which does not change significantly across interior structure models. Our models predict a much narrower set of orientations than we observe, perhaps because we have effectively treated every point along the TSFs as an independent point of nucleation. In reality, there may have been fewer nucleation points from which fractures propagated and interacted to form the system of TSFs we observe today. In addition, shear motions along existing fault segments could form new cracks that do not correspond to the orientations of the tensile stresses (e.g., Marshall and Kattenhorn, 2005). We have also made the simplifying assumption that failure occurs at the exact value of the threshold we impose. If we instead took a probabilistic approach, assuming that failure at the threshold was most likely but that fail-

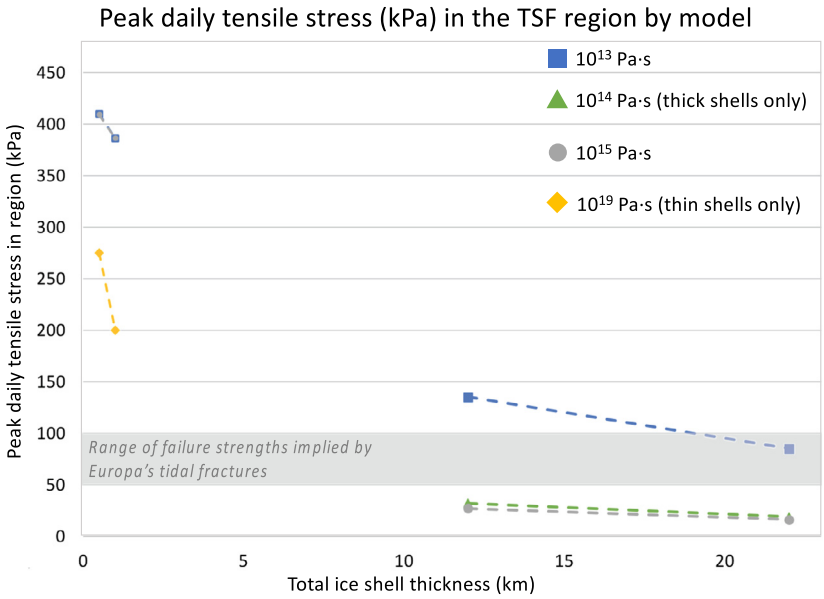

Fig. 5. The regional peak stress (RPS) calculated across all of the TSF points for a subset of models illustrates the trends in stress magnitude with shell thickness and ductile shell viscosity (symbols/colors). The hashed lines are inferred trends; we only computed stresses for the cases marked with symbols. All cases shown include a brittle layer that is 10% of the total shell thickness. RPS magnitudes increase with decreasing shell thickness. Only the thickest shells with ductile ice viscosities $\geq 10^{14}$ Pa·s produce stresses lower than the magnitudes inferred from Europa's fractures (shaded box). Thinner shells are also less sensitive to the ductile ice viscosity than thicker shells. We, thus, infer that the north polar region of Enceladus must be >10 km thick and have a ductile ice viscosity of $\geq 10^{14}$ Pa·s to explain the lack of tidal-tectonic activity as compared with the south pole.

ure at lower values was also possible, we would produce a broader range of orientations.

It is also possible that the ice shell has changed thickness or viscosity over time, which would lead to differences in tidal stress magnitudes and a slight shift in the predicted orientations. We have selected prominent and continuous branches of the TSFs, which are among the youngest features on Enceladus, limiting the likelihood of large changes in the ice shell as they formed. However, the fractures overlain by the TSFs could have formed at an earlier epoch, which may explain why their orientations, morphology, and cross-cutting relationships are so different from the TSFs.

Our work does not specifically address the formation of the older fracture systems within the SPT, its bounding system of fractures, or its topography. Yin and Pappalardo (2015) have offered a scenario that can generate much of the observed SPT geology. However, given that the orientations of the TSFs can be fit extremely well with a simple model of tensile cracks forming in response to tidal stress, and that tensile fractures are more consistent with the TSFs acting as plume conduits, we argue that the TSFs did not form as a result of strike-slip motion during the evolution of the SPT, suggested by Yin and Pappalardo (2015), although other aspects may well have taken place.

5.2. Stress sources and magnitudes

Our model includes only the effects of eccentricity, and with our threshold failure assumption, we can match the TSF orientations extremely well. Hence, we have no need to invoke rotation of the ice shell. In fact, any stress from NSR would combine with eccentricity-driven stresses and change the prevailing orientation of the stress field, likely creating a worse fit to the observations. Similarly, adding stress from an ice shell of variable thickness over a pressurized ocean (Johnston and Montesi, 2017) would generate a different stress pattern than diurnal tides, which seems unlikely to improve fits to the observations.

The volumetric changes that occur as an ice shell cools and thickens will also generate stress, independent of whether the ocean is pressurized (Nimmo, 2004). The cooling stresses are uniform, so they do not alter the pattern of stress at the surface, and can be sufficiently large to exceed the failure strength of laboratory ice, e.g., >1 MPa (Schulson, 2006). In this case, eccentricity-driven tides would control fracture orientations, and all of the stress magnitudes would slowly increase by the same amount until the combination of diurnal tidal stress and cooling stress exceeds the failure strength of the ice shell. However, cooling would increase stresses globally, making it more challenging to explain the limited fracturing at the north pole and elsewhere on Enceladus. This idea is also less compatible with the threshold failure assumption, unless significant stress from cooling can accumulate within one orbit. Otherwise, the first time the combined stresses should exceed the failure threshold should be when the daily tidal stress reaches its maximum.

Beuthe (2018) finds that an ice shell that is thinner at the poles than the equator will experience an enhancement in tidal stress magnitudes at the poles, while stress orientations are largely unaffected. Specifically, he determined that a convecting ice shell with thickness of 30 km at the equator, 15 km at the north pole, and 7 km at the south pole, and a melting point viscosity of 10^{13} Pa·s, would generate stresses at the south pole that are 12x larger than an ice shell that is 23 km everywhere. For comparison, our uniform thickness model captures only the 2-3x increase in tidal stress between a 22 km shell and a 5 km shell, which suggest an additional factor of 4 increase in stress may be introduced by the shell thickness variations. Beuthe (2018) finds the enhancement at the north pole is only 2x, in part because the ice shell is thicker there than at the south pole.

As another point of comparison, we calculated stress in a 22 km globally uniform thickness ice shell with a ductile ice viscosity of 10^{13} Pa·s (marked F in Table 2), which is the most similar in our suite of models to the uniform thickness ice shell of Beuthe (2018). His results suggest that, if the south pole were only 7 km, the tidal stresses could increase from the ~50 kPa we predict to ~600 kPa, while the north pole would achieve stresses of ~100 kPa. If the ice shell were even thinner at the south pole, such amplifications might allow the tidal stresses in the south pole to exceed the 1 MPa failure strength of laboratory ice while still matching the ob-

served TSF orientations and being consistent with the threshold failure assumption.

5.3. The polar dichotomy

We must now consider how tidal fracturing is inhibited at the north pole, given the observational constraints. First, we will assume that Enceladus' ice shell can fracture at ~100 kPa, as inferred from Europa. Only thick shell models with ductile ice viscosities of $\geq 10^{14}$ Pa·s produce stresses <50 kPa, and these magnitudes are likely an under estimate due to the amplification described above. Hence, the ice shell must be relatively thick and cool at the north pole to inhibit tidal fracturing. At the south pole, the ice shell could also be fairly thick and still achieve large tidal stresses, but only if the entire ductile layer maintains a viscosity of 10^{13} Pa·s, which is lower than the 3×10^{14} Pa·s melting point viscosity inferred by Cadek et al. (2019). If the south polar region is only a few km thick or less (e.g., Cadek et al., 2016; Beuthe et al., 2016; Cadek et al., 2019), we would predict failure for all of the values of lower-shell viscosity we tested. Because such a thin shell would likely be conducting, the cases with viscosities of 10^{15} or 10^{19} Pa·s are likely more plausible than 10^{13} Pa·s, which is also consistent with the constraint on melting-point viscosity. With these thinner shells at the south pole, an ice shell 10 km thicker at the north pole would experience comparatively lower tidal stresses, although it would also need to have a viscosity $>10^{13}$ Pa·s to ensure low stresses. Given the constraints from the gravity data, and inferred melting point viscosity, we favor the interpretation that the ice shell at the south pole of Enceladus is $\leq$5 km, while at the north pole it is $\geq$10 km with a viscosity of 10^{14} Pa·s or higher.

An alternative solution is that the ice shell fails at $\geq$1 MPa, and that tidal stress magnitudes are enhanced beyond what we have calculated due to the locally thinner regions at the poles. Beuthe (2018) has only calculated stress enhancements for one thickness profile at Enceladus, but combining those results with ours, we infer that the ice shell would need to be thinner than the 7 km used by Beuthe (2019) at the south pole in order for the tidal stress to exceed 1 MPa while remaining thicker than 7 km at the north pole to avoid fracturing there. Hence, with either assumption as to the strength of Enceladus' ice shell, we find that the difference in shell thickness between the two poles is sufficient to explain the dichotomy in tectonic activity and supports an ice shell that is less than 5-7 km at the south pole and "of order" 10 km thicker in the north pole than the south. These conclusions are fully compatible with other constraints on Enceladus' ice shell thickness.

5.4. Enceladus' evolution

We will now offer a speculative hypothesis as to the history of Enceladus that would be compatible with our results, as well as the global geologic record. If Enceladus were once frozen, its shell grounded against a monolithic rocky core, tidal dissipation would be largest in zones centered at the equator and concentrated along the lines of longitude at the sub and anti-Saturnian points and the leading and trailing nodes (as shown in Fig. 3A of Roberts, 2015). Because the ice shell would be elongated along the tidal axis, due to the gravitation pull of Saturn, it would be somewhat thicker at the sub and anti-Saturnian points than at the leading and trailing nodes. The difference in thickness, and steeper thermal profile, may thus lead to enhanced heating and melting at the base of the ice shell within the leading and trailing dissipation zones. The combination of thinner ice and the presence of regional, subsurface melt zones, would generate larger tidal stresses than the surrounding regions, eventually kicking off the deformation and fracturing that formed the observed leading and trailing tectonized regions.

If melting became widespread, such that there was even a very thin decoupling layer of liquid between the rocky interior and overlying ice shell, the shell would no longer be grounded. Enceladus' dissipation pattern would transition to that of a global ocean, in which heating is highest at the poles and lowest at the equator (e.g., Roberts, 2015). The equatorial regions would cool and thicken, reducing tidal stresses and shutting down tectonic activity there. Instead, melting, deformation, and tectonic activity would be focused at poles. The south pole would thin, enhancing tidal stresses, and eventually form cracks that could penetrate to the ocean, creating plumes and potentially relieving stress. The ice shell at the north pole may have also thinned over this time period, which would explain why it is thinner than at the equator. As we have shown, the thicker north pole would experience lower tidal stresses, explaining its lack of tectonic activity, although the reason it thinned more slowly than the south pole remains a mystery. This speculative history allows for the possibility that the north pole is currently thinning, perhaps explaining the recent fractures observed there.

No studies have yet addressed how tidal heating evolves in an ice shell of variable thickness as it transitions from frozen to overlying a global ocean. Beuthe (2019) examined tidal heating in an ice shell with lateral thickness variations and reported that the thinnest part(s) of an ice shell will experience the highest tidal heating, which supports our idea that the leading and trailing regions at the equator could warm and melt faster than the sub and anti-Saturn points. However, that model included a global ocean, not a grounded ice shell. Examining the tidal and thermal evolution of an initially frozen Enceladus would be a valuable avenue of future work.

6. Conclusions

We find that the orientations of the Tiger Stripe Fractures are well-explained as tensile fractures that formed at a consistent stress threshold in response to eccentricity tidal stresses. The inferred 10 km difference in shell thickness between the north and south poles of Enceladus can create a difference in tidal stress magnitudes sufficient to explain tidally-driven fractures in the south but not the north, particularly if the ice shell is less than ~5 km at the south pole. In thin shells, the tidal stress magnitudes are 100s of kPa, lower than the laboratory-derived failure threshold of ice but larger than those inferred from tidally-driven fractures on Europa. Enhancements in diurnal tidal stress caused by shell thickness variations (Beuthe, 2018) may allow the south polar region to exceed a 1 MPa failure threshold, while preserving the orientations we report here. The enhancement would need to be lower at the north pole to explain the lack of tectonic activity there, which would occur for the differences in shell thickness we have reported. Based on these results, we have offered a hypothesis to explain the formation of Enceladus' diverse geology through time, which we hope will spur continued interest and investigation into this enigmatic moon.

Author contributions

A. Rhoden computed tidal stresses and orientation predictions, conducted the analysis, and led manuscript and figure preparation. Stresses were computed based on inputs from a numerical code written and run by W. Henning. T. Hurford assisted with all aspects of the tidal stress calculations and with data and manuscript preparation. J. Spitale obtained latitude, longitude, and orientation data from Cassini images and assisted with manuscript preparation. M. Bland assisted with selection of interior structure models. S. Sajous developed key software for the data analysis.

Declaration of competing interest

The authors declare that they have no known competing financial interests or personal relationships that could have appeared to influence the work reported in this paper.

Acknowledgements

This work was supported by NASA Cassini Data Analysis Program grants NNX15AL09G and 80NSSC19K0891. The manuscript benefitted from discussions with members of the Ocean Worlds Cooperative and Matthew E. Walker, as well as comments from Marissa Cameron, Mikael Beuthe, Paul Helfenstein, Bill McKinnon, and an anonymous reviewer. The results in this paper can be reproduced using the equations reported herein and in the cited references, using the parameters values given in the tables, references, and supporting online materials.

Appendix A. Supplementary material

Supplementary material related to this article can be found online at https://doi.org/10.1016/j.epsl.2020.116389.

References

Behounkova, M., Tobie, G., Cadek, O., Choblet, G., Porco, C., Nimmo, F., 2015. Timing of water plume eruptions on Enceladus explained by interior viscosity structure. Nat. Geosci. https://doi.org/10.1038/NGEO2475.

Behounkova, M., Soucek, O., Hron, J., Cadek, O., 2017. Plume activity and tidal deformation on Enceladus influenced by faults and variable ice shell thickness. Astrobiology. https://doi.org/10.1089/ast.2016.1629.

Beuthe, M., Rivoldini, A., Trinh, A., 2016. Enceladus's and Dione's floating ice shells supported by minimum stress isostasy. Geophys. Res. Lett. https://doi.org/10.1002/2016GL070650.

Beuthe, M., 2018. Enceladus's crust as a non-uniform thin shell: I tidal deformation. Icarus 302, 145–174.

Beuthe, M., 2019. Enceladus's crust as a non-uniform thin shell II: tidal dissipation. Icarus 332, 66–91.

Cadek, O., Tobie, G., Van Hoolst, T., Masse, M., Choblet, G., Lefevre, A., Mitri, G., Baland, R.-M., Behounkova, M., Bourgeois, O., Trihn, A., 2016. Enceladus' internal ocean and ice shell constrained from Cassini gravity, shape, and libration data. Geophys. Res. Lett. 43, 5653–5660.

Cadek, O., Soucek, O., Behounkova, M., Choblet, G., Tobie, G., Hron, J., 2019. Long-term stability of Enceladus' uneven ice shell. Icarus 319, 476–484.

Crow-Willard, E.N., Pappalardo, R.T., 2015. Structural mapping of Enceladus and implications for formation of tectonized regions. J. Geophys. Res. 120, 928–950.

Hedman, M.M., Gosmeyer, C.M., Nicholson, P.D., Sotin, C., Brown, R.H., Clark, R.N., Baines, K.H., Buratti, B.J., Showalter, M.R., 2013. An observed correlation between plume activity and tidal stresses on Enceladus. Nature 500, 182–184.

Helfenstein, P., Porco, C.C., 2015. Enceladus' geysers: relation to geological features. Astron. J. 150, 96–129.

Hemingway, D.J., Rudolph, M.L., Manga, M., 2020. Cascading parallel fractures on Enceladus. Nat. Astron. https://doi.org/10.1038/s41550-019-0958-x.

Hurford, T.A., Helfenstein, P., Hoppa, G.V., Greenberg, R., Bills, B.G., 2007. Eruptions arising from tidally controlled periodic openings of rifts on Enceladus. Nature 447, 292–294.

Iess, L., Stevenson, D.J., Parisi, M., Hemingway, D., Jacobson, R.A., Lunine, J.I., Nimmo, F., Armstrong, J.W., Asmar, S.W., Ducci, M., Tortora, P., 2014. The gravity field and interior structure of Enceladus. Science 344, 77–80.

Jara-Orué, H.M., Vermeersen, B.L., 2011. Effects of low-viscous layers and a non-zero obliquity on surface stresses induced by diurnal tides and non-synchronous rotation: the case of Europa. Icarus 215, 417–438.

Johnston, S.A., Montesi, L.G.J., 2017. The impact of a pressurized regional sea or global ocean on stresses on Enceladus. J. Geophys. Res. 122, 1258–1275.

Kalousova, K., Soucek, O., Cadek, O., 2012. Deformation of an elastic shell with variable thickness: a comparison of different methods. Geophys. J. 190, 726–744.

Kinczyk, M.J., Byrne, P.K., Collins, G.C., Patterson, G.W., Bohnenstiehl, D.R., 2017. Stress risers in Enceladus' cratered terrain. In: 50th LPSC. abstract 2132.

Kite, E.S., Rubin, A.M., 2016. Sustained eruptions on Enceladus explained by turbulent dissipation in tiger stripes. Proc. Natl. Acad. Sci. 113, 3972–3975.

Marshall, S.T., Kattenhorn, S.A., 2005. A revised model for cycloid growth mechanics on Europa: evidence from surface morphologies and geometries. Icarus 177, 341–366.

Martin, E.S., 2016. The distribution and characterization of strike-slip faults on Enceladus. Geophys. Res. Lett. 43, 2456–2464.

McKinnon, W.B., 2015. Effect of Enceladus' rapid synchronous spin on interpretation of Cassini gravity. Geophys. Res. Lett. 42, 2137–2143.

Nimmo, F., 2004. Stresses in cooling viscoelastic ice shells: application to Europa. J. Geophys. Res. 109, 12001–12010.

Nimmo, F., Spencer, J.R., Pappalardo, R.T., Mullen, M.E., 2007. Shear heating as the origin of the plumes and heat flux on Enceladus. Nature 447, 289–291.

Nimmo, F., Porco, C., Mitchell, C., 2014. Tidally modulated eruptions on Enceladus: Cassini ISS observations and models. Astron. J. 148, 1–14.

Patthoff, D.A., Kattenhorn, S.A., 2011. A fracture history on Enceladus provides evidence for a global ocean. Geophys. Res. Lett. 38, L18201.

Patthoff, D.A., Kattenhorn, S.A., Cooper, C.M., 2019. Implications of nonsynchronous rotation on the deformation history and ice properties in the South polar terrain of Enceladus.

Porco, C.C., Helfenstein, P., Thomas, P.C., 22 colleagues, 2006. Cassini observes the active South pole of Enceladus. Science 311, 1393–1401.

Porco, C., DiNino, D., Nimmo, F., 2014. How the geysers, tidal stresses, and thermal emission across the South pole terrain of Enceladus are related. Astron. J. 148, 1–24.

Rhoden, A.R., Hurford, T.A., 2013. Lineament azimuths on Europa: implications for obliquity and non-synchronous rotation. Icarus 226, 841–859.

Rhoden, A.R., Henning, W., Hurford, T.A., Hamilton, D.P., 2015. The interior and orbital evolution of Charon as preserved in its geologic record. Icarus 246, 11–20.

Rhoden, A.R., Henning, W., Hurford, T.A., Patthoff, D.A., Tajeddine, R., 2017. The implications of tides on the Mimas ocean hypothesis. J. Geophys. Res. 122, 400–410.

Roberts, J.H., 2015. The fluffy core of Enceladus. Icarus 258, 54–66.

Schulson, E.M., 2006. The fracture of water ice 1h: a short overview. Meteorit. Planet. Sci. 41, 1497–1508.

Spencer, J.R., Pearl, J.C., Segura, M., 7 colleagues, 2006. Cassini encounters Enceladus: background and the discovery of a South polar hot spot. Science 311, 1401–1405.

Spitale, J.N., Porco, C.C., 2007. Association of the jets of Enceladus with the warmest regions on its South-polar fractures. Nature 449, 695–697.

Spitale, J.N., Hurford, T.A., Rhoden, A.R., Berkson, E.E., Platts, S.S., 2015. Curtain eruptions from Enceladus' South-polar terrain. Nature 521, 57–60.

Thomas, P.C., Tajeddine, R., Tiscareno, M.S., Burns, J.A., Joseph, J., Loredo, T.J., Helfenstein, P., Porco, C., 2016. Enceladus's measured physical libration requires a global subsurface ocean. Icarus 264, 37–47.

Wahr, J., Selvans, Z.A., Mullen, M.E., Barr, A.C., Collins, G.C., Selvans, M., Pappalardo, R.T., 2009. Modeling stresses on satellites due to nonsynchronous rotation and orbital eccentricity using gravitational potential theory. Icarus 200, 188–206.

Yin, A., Pappalardo, R.T., 2015. Gravitational spreading, bookshelf faulting, and tectonic evolution of the South polar terrain of Saturn's moon Enceladus. Icarus 260, 409–439.

Yin, A., Zuza, A.V., Pappalardo, R.T., 2016. Mechanics of evenly spaced strike-slip faults and its implications for the formation of the tiger-stripe fractures on Saturn's moon Enceladus. Icarus 266, 204–216.